THE JOURNAL OF PHYSICAL CHEMISTRY C

Article

A Hybrid Molecular Dynamics/Multi Conformer Continuum Electrostatics (MD/MCCE) Approach for the Determination of Surface Charge of Nanomaterials

Jiewei Hong, Robert J Hamers, Joel A. Pedersen, and Qiang Cui

J. Phys. Chem. C, **Just Accepted Manuscript** • DOI: 10.1021/acs.jpcc.6b11537 • Publication Date (Web): 27 Jan 2017

ACS Publications

The Journal of Physical Chemistry C is published by the American Chemical Society. 1155 Sixteenth Street N.W., Washington, DC 20036

A Hybrid Molecular Dynamics/Multi Conformer Continuum Electrostatics (MD/MCCE) Approach for the Determination of Surface Charge of Nanomaterials

Jiewei Hong,[†] Robert J. Hamers,[‡] Joel A. Pedersen,[¶] and Qiang Cui[*,†]

†*Department of Chemistry and Theoretical Chemistry Institute, University of Wisconsin-Madison, 1101 University Avenue, Madison, WI 53706*

‡*Department of Chemistry, University of Wisconsin-Madison, 1101 University Avenue, Madison, WI 53706*

¶*Departments of Soil Science, Civil & Environmental Engineering, and Chemistry, University of Wisconsin-Madison, 1525 Observatory Drive, Madison, WI 53706*

E-mail: cui@chem.wisc.edu, Tel:(+1)-608-332-6584

Abstract

The surface charge of nanomaterials determines their stability in solution and interaction with other molecules and surfaces, yet experimental determination of surface charge of complex nanomaterials is not straightforward. We propose a hybrid approach that iteratively integrates explicit solvent molecular dynamics simulations and a multi-conformer continuum electrostatic model (MCCE) to efficiently sample the configurational and titration spaces of surface ligands of nanomaterials. Test calculations of model systems indicate that the iterative approach converges rapidly even for systems that contain hundreds of titratable sites, making the approach complementary

to more elaborate methods such as explicit solvent-based constant pH molecular dynamics. The hybrid method is applied to analyze the pK_a distribution of alkyl amines attached to a carbon-based nanoparticle as a function of ligand density, nanoparticle surface curvature and ligand heterogeneity. The results indicate that functionalization strategies can modulate the pK_a of surface ligands, and therefore charge properties of nanomaterials (e.g., surface charge, charge capacitance). The hybrid computational approach makes a major step towards guiding the design of nanomaterials with desired charge properties.

1 Introduction

Nanotechnology is playing increasingly prominent roles in the society. With well-controlled size, shape and composition, nanomaterials can have unique physical and chemical properties that make them well suited in a broad range of applications such as energy storage,[1] water treatment,[2–4] imaging,[5–7] drug delivery and diagnostics[8–11] and electronic displays.[12,13] On the other hand, the small size, large surface area and possibly high chemical reactivity of nanomaterials raise concern about their potential to cause deleterious environmental and health impacts. Therefore, significant efforts have been made to determine the environmental behavior and toxicity of nanomaterials.[14–18] Due to the complexity of nano/bio interfaces, however, it is often not straightforward to understand the molecular-level mechanisms that underlie the observed toxicities.[19–21] Along this line, a tight integration between multi-faceted experimental studies and computational analyses is required to determine the causal relationships between physicochemical properties of nanomaterials and their impacts on the environment and biological systems.[22,23]

One of the key physicochemical properties in this context is the surface charge distribution of nanomaterials, which strongly influences how nanomaterials interact with each other and with surrounding (bio)molecules, such as proteins and lipid membrane.[24–28] For example, several studies have indicated that positively charged nanoparticles are more toxic than negatively charged nanoparticles to organisms such as bacteria[29] and *Daphnia magna*.[30] Thus it is important to be able to control and determine the amount of surface charge of nanomaterials. A quantitative determination of surface charge, however, is far from straightforward. First, nanomaterials are often functionalized with organic ligands to either enhance suspension stability or to modulate chemical reactivity, and these ligands often include titratable groups. When the ligand density is high, the titrable groups are coupled electrostatically and lead to complex pH dependence of the surface charge.[31] Therefore, although ligand density can be measured experimentally using, for example, X-ray photoelectron spectroscopy,[32,33] microscopic charge state information is not readily available. Second, charged nanomateri-

als interact strongly with other charged moieties in the surrounding environment, such as electrolyte ions, to form the electrical double layer.[34,35] When the surface morphology of the nanomaterials is rough at the molecular scale, quantitative interpretation of experimental observables such as ζ potential from electrokinetic measurements[36,37] and surface potential measured by second harmonic generation[38–40] is not straightforward.

Theory and molecular simulations can potentially provide important insights in this regard. With relatively simple models for the nanomaterials (e.g., a homogeneous sphere) and ligands, one can analyze the surface charge distribution as a function of pH, salt concentration and nanoparticle size (or curvature) using either a semi-analytical model[41] or Monte Carlo simulations.[42,43] For many applications, atomically detailed models for the nanomaterials, ligands and the surrounding environment are desirable. In such cases, a simulation method is needed that is able to cope with the characteristics of functionalized nanomaterials. For example, for biophysical applications, the same issue of understanding the titration behavior of proteins and nucleic acids as a functions of pH has led to the development of computational techniques[44] that range from implicit solvent models[45–48] to generalized ensemble-based explicit solvent free energy methods.[49–53] Among them, the constant pH molecular dynamics approach has recently been applied to study the microscopic titration behavior of a small gold nanoparticle (with a diameter of $\sim$2.2 nm) functionalized with *p*-mercaptobenzoic acid;[54] good agreement was found between the predicted amount of ionized ligands and values measured using infrared spectroscopy. The constant pH molecular dynamics approach, however, requires an extensive sampling of the expanded ensemble that includes the titration variables; therefore, for applications that involve a large number (e.g., hundreds) of titratable groups, which are often encountered in functionalized nanomaterials (see examples below), achieving convergence poses a serious challenge. The presence of a large number of charged ligands also leads to other technical difficulties, such as dealing with net-charge fluctuations using Particle-Mesh-Ewald summations[55–57] and finite size effects associated with the need to include a large number of ions to properly represent a specific bulk

salt concentration.

Motivated by these considerations, we propose to adopt a simple hybrid scheme that integrates molecular dynamics (MD) and Monte Carlo simulations, which samples the configuration and titration space using explicit solvent and continuum electrostatics models, respectively. The approach is similar in spirit to previous studies of protein,[58,59] polyelectrolyte[60] and lipid membranes,[61,62] although, to our knowledge, the specific continuum electrostatics model (Multi-Configuration-Continuum-Electrostatics, MCCE[48,63]) has not been integrated with MD sampling in the same way. Our approach also serves to extend the application of MCCE, which was developed to study proteins, to complex nanomaterials.

In the following, we first present the hybrid MD/MCCE protocol, including a brief review of the MCCE approach and the required parameters. Next, we apply the MD/MCCE protocol to study the titration behavior of several model systems to illustrate the versatility of the methodology; we explore how ligand density, nanoparticle surface curvature and ligand heterogeneity impact the titration behavior of surface ligands and therefore the surface charge distribution of the nanoparticle. We conclude with a few remarks.

2 Method and Computational Setup

Conceptually, the hybrid MD/MCCE approach is straightforward: explicit solvent MD is used to sample the configurations of the nanomaterial and its surface ligands, and the MCCE approach is employed to sample the microscopic protonation states of titratable groups; iteration between the MD and MCCE calculations leads to self-consistency between distributions in the configuration space and protonation states. In the following, we first provide a brief review for the MCCE approach and its adaptation to functionalized nanomaterials; then, we specify a number of technical details of the hybrid MD/MCCE protocol.

2.1 Brief Review of Multi-Conformer Continuum Electrostatics (MCCE)

MCCE is a well-established technique for computing pK_a and reduction potential for residues in proteins.[48,63] It targets pK_a and reduction potential *shifts* for residues in a protein relative to the relevant reference compounds in solution, and it is based on the approximation that such shifts are dominated by the difference in electrostatic free energy of the residues in different environments. In addition, for each titratable group of interest, MCCE also considers multiple conformational degrees of freedom based on a rotamer library search, local minimizations and a pruning process based on rotamer packing and conformer clustering. The selected conformers are subjected to Metropolis Monte Carlo sampling[64] to generate the Boltzmann distribution; in addition to configurational sampling, the Monte Carlo moves also consider changing the ionization state (or redox state) of titratable residues. The free energy used in the Monte Carlo sampling over the microstates (one conformer of each residue makes up a microstate x) is given by,

$$\begin{aligned}\Delta G^x = \sum_{i=1}^{M} \delta_{x,i}\{&[2.3 m_i k_B T(pH - pK_{sol,i}) + n_i F(E_h - E_{m\ sol,i})] \\ &+ (\Delta\Delta G_{rxn,i} + \Delta G^{CE}_{bkbn,i} + \Delta G^{LJ}_{bkbn} + \Delta G_{torsion,i} + \Delta\Delta G_{SAS,i}) \\ &+ \sum_{j=i+1}^{M} \delta_{x,j}[\Delta G^{CE}_{ij} + \Delta G^{LJ}_{ij}]\}.\end{aligned} \tag{1}$$

Here M is the total number of conformations; $\delta_{x,i/j}$ is 1 if conformer i/j is present in the microstate x and 0 otherwise; m_i is 1 for bases, -1 for acids and 0 for neutral conformers; n_i is the number of electrons transferred to a redox-active ligand; k_BT and F are the standard thermal energy and Faraday's constant, respectively. pH and E_h specifies the solution acidity and electrode potential, respectively. The p$K_{sol,i}$ and $E_{m\ sol,i}$ are the solution pK_a and mid-potential for the relevant reference compounds, respectively, and therefore do not depend on the conformers. The second line of Eq.1 describes the conformer self-energies and

contain reaction field or solvation free energy ($\Delta\Delta G_{rxn,i}$), electrostatic and Lennard-Jones interactions with protein backbones ($\Delta G^{CE}_{bkbn,i}$, ΔG^{LJ}_{bkbn}), torsional energy ($\Delta G_{torsion,i}$) and a surface-area term ($\Delta\Delta G_{SAS,i}$). The third line of Eq. 1 contains the pairwise electrostatic and Lennard-Jones interactions among conformers present in the microstate x.

Using this free energy expression, MCCE conducts Monte Carlo sampling in both protonation and conformer spaces over different solution (pH, and when redox processes are involved, also E_h) conditions. Upon convergence, the pH-dependent population of each titratable site in the ionized (charged) state is fit to the Henderson-Hasselbalch equation to obtain the pK_a value:

$$\langle P_{ionized} \rangle = \frac{10^{-mn(pH-pK_a)}}{1+10^{-mn(pH-pK_a)}}, \tag{2}$$

where m is -1 for acid and +1 for base, and n is the Hill coefficient. As discussed thoroughly in Ref.,[31] such defined pK_a values do not rigorously reflect well-defined equilibrium constants; i.e., they do not correspond to either microscopic, or macroscopic, or quasisite pK_a values, which have clear statistical mechanics definitions for polyprotic acids that feature strongly coupled sites. Nevertheless, for a nanoparticle that features hundreds of titratable sites that are not easily distinguishable from each other (as opposed to the situation in a protein), such mean-field like pK values are perhaps most straightforward to characterize the tendency for the ligands to be protonated; alternatively, one may directly monitor the number of protonated sites at each pH, as we also show below. For additional discussion of technical details, see the original MCCE papers.[48,63]

For nanomaterials applications, we can readily adopt Eq.1 for MCCE calculations if we identify the proper solution reference compounds, and have a set of force field parameters for the computation of electrostatic and Lennard-Jones interactions, as well as for the solvation (reaction field) free energies. The terms related to "protein backbones" ($\Delta G^{CE}_{bkbn,i}$; ΔG^{LJ}_{bkbn}) are replaced by interactions between titratable ligands and nanomaterials. For the solvation free energy ($\Delta\Delta G_{rxn,i}$) calculations, Poisson-Boltzmann equations[34,65] are solved, which requires the specification of the dielectric map for the various regions of the solvated system; the

dielectric constant appropriate for the nanomaterials can be rather different from that for a protein.[66] We note that although the ligand density in some systems studied here reaches 9 molecules/nm^2, the charge density for conditions of interest is substantially lower (see below), thus the Poisson-Boltzmann model remains valid in our applications; we do not observe major differences between linear and non-linear Poisson-Boltzmann results for cases of interest.

2.2 A Hybrid Molecular Dynamics/MCCE Approach

The rotamer sampling makes MCCE more robust for pK_a/reduction potential calculations than those based on a single or a few protein conformation(s).[67,68] Nevertheless, the degree of sampling in MCCE is still rather limited; for proteins, for example, the backbone structure is usually frozen, which prevents global conformational transitions coupled to the titration process. For nanomaterials applications, more extensive conformational sampling of the ligands (and possibly nanomaterials, if not rigid) is also desirable to ensure accurate prediction of pK_a and redox potential values; this is particularly important, for example, when the titratable ligands are part of a polymer anchored to the nanomaterials' surface through non-covalent interactions.

Therefore, we propose an iterative, hybrid MD/MCCE approach. As illustrated in the scheme in Fig. 1, starting with an initial guess of protonation/redox pattern, explicit solvent molecular dynamics calculations are conducted to sample the ligand configurations. Following the MD simulation, explicit water and ions are removed and MCCE is used to compute the pK_a/reduction potential values of the ligands; the results are used to assign a new set of charge pattern under the solution condition of interest; e.g., the computed pK_a values determine the total number of protonated sites ($n_{H^+} = \sum_i \langle P_{i,ionized} \rangle$) at a specific pH value, we then randomly select n_{H^+} titratable sites to be protonated. After adjusting the explicit solvent simulation setup based on the updated protonation pattern, the system is subject to another round of MD simulation, which in turn is followed by another round of MCCE

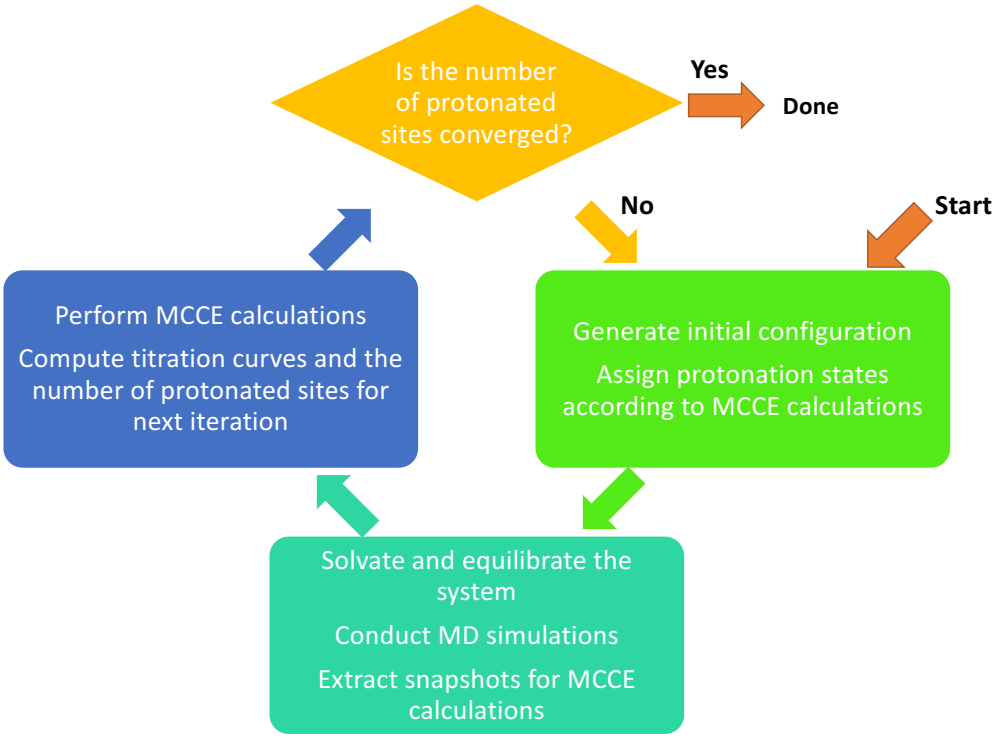

Figure 1: A scheme that illustrates the iterative protocol that integrates explicit solvent molecular dynamics and multi-conformer continuum electrostatics (MCCE) model to efficiently sample the configurational space and titration states of functionalized nanomaterials.

calculation. This process is iterated until the computed pK_a /reduction potential values reach convergence.

Compared to constant pH MD simulations,[49–52,59] our hybrid approach is more approximate since the key free energy quantities (Eq. 1) are computed based on a continuum electrostatic and implicit solvent framework; in this regard, we note that MCCE has been extensively benchmarked with protein pK_a and reduction potential calculations and therefore is considered to be one of the most reliable continuum electrostatic models.[63] The gain is clearly in the computational efficiency; as shown below, the MCCE approach is readily applicable even when a large number (e.g., >400) of titratable sites are present. The integration of MD and MCCE also further enhances the degree of conformational sampling relative to these methods alone. Without the need to change the total charge of the system in each MD simulation, we also avoid complications associated with Particle-Mesh-Ewald calculations for systems with a large net charge. We choose to employ explicit solvent/ions MD simulations rather than implicit solvent models because the latter require specifically parameterized ion models in the same framework.

In realistic applications, important practical issues include whether the hybrid MD/MCCE calculations reach proper convergence and what factors control the speed of convergence; for example, should one conduct long MD simulations following each round of MCCE computation or short MD simulations are more appropriate? Long MD simulations appear necessary to fully relax ligand configurations following a change of protonation pattern. On the other hand, short MD simulations connected by changes in protonation pattern better resemble constant pH simulations. Therefore, convergence needs to be carefully monitored in practical applications (see example and discussion in Sect.3).

2.3 Computational Setup

To test the hybrid MD/MCCE approach, we study the titration behaviors of a group of alkyl amines attached to a model carbon nanoparticle solvated in water; the model nanoparticle

contains 446 carbon atoms evenly distributed on the surface of a sphere of 4 nm diameter. The model is not meant to explicitly mimic a realistic carbon dot or nanodiamond since our goal is to explore the convergence behavior of the hybrid MD/MCCE protocol and qualitative trends in the titration behavior of surface ligands. The internal structure of the nanoparticle is frozen during MD simulations. To explore the effect of nanoparticle surface curvature, we study ligands attached to carbon sheets with a specific set of radii of curvature. Each carbon sheet contains 100 carbon atoms initially arranged in a square lattice; the positions of the carbon atoms on a curved sheet are then determined by projecting the planar model onto a sphere of the corresponding radius of curvature.

For the MD simulations, the carbon sphere/sheet is described using a set of charge-neutral Lennard-Jones particles; the parameters are taken from the CHARMM36-cgenff[69] force field for propene; parameters for the ligands (alkyl amines) are constructed based on the lysine sidechain (in both protonated and deprotonated states) in the CHARMM36 force field for proteins.[70] Water is described using a modified TIP3P model;[71,72] ions are introduced to neutralize the total charge of the system and they are described using the CHARMM36 force field. For the MD simulations, the NVT ensemble is used and the temperature is set to 300 K using the Nose-Hoover thermostat;[73,74] NPT ensemble might be more preferable when directly comparing to experimental measurements, so that change in system density due to different charge states of the nanoparticle is explicitly considered. Periodic boundary conditions are used and the cubic cell has the dimension of 80 Å for the carbon nanoparticle and 40 Å for the nanosheet. Electrostatic interactions are treated with Particle-Mesh-Ewald[75] with a grid size of ∼1 Å; van der Waals interactions are treated with a 12 Å cutoff and a sigmoidal switching function between 10 and 12 Å. Bonds involving hydrogen are constrained using SHAKE,[76] which allows an integration time step of 2 fs. The typical sampling time for each iteration of MD simulation is about 10 ns, which is sufficient for the key structural properties and MCCE pK_a predictions to converge (see **Supporting Information**). To avoid very high charges on the functionalized nanoparticle, MD simulations are conducted at the pH

value of 9; this is convenient for the current purpose of exploring the applicability of the hybrid scheme, while in realistic applications it is preferable to conduct the MD simulations at the pH of interest.[31,77] The simulations for the nanosheet is carried out with CHARMM 39a1,[78] while those for the nanoparticle is done with NAMD2.10.[79]

From each MD trajectory, snapshots are extracted every 0.2 ns to obtain 50 snapshots; for each snapshot, MCCE calculation is performed and the reported pK_a results are averaged over the 50 independent calculations. In each MCCE calculation, the alkyl amines are treated as titratable residues. Six rotamers are generated for each bond rotation in the alkyl amine, and rotamers with large steric interactions or a large solvent accessible surface are removed; afterwards, repacking is performed to further prune the rotamers. In the continuum electrostatic calculations, the solute dielectric constant is set to 8.0 as recommended for MCCE calculations for proteins; using a value of 4.0 does not change the results to any significant degree (<2%); the solvent dielectric constant is 80.0, and the solvent probe radius is 1.4 Å. The salt concentration in the Poisson-Boltzmann calculations is set to be the same as in the explicit solvent MD simulations; the partial charges and atomic radii for the Poisson-Boltzmann calculations are also taken from the explicit MD simulations. For the titration calculations, pH is varied from -10 to 14 at an interval of 1 pH unit. At each pH value, one first conducts (1,000× # of conformers) steps of annealing, which is followed by (5,000× # of conformers) steps of Monte Carlo equilibration. Then five independent sets of Monte Carlo simulations are performed, with each sampling (20,000× # of conformers) steps. The results are averaged to compute the occupancy of each titratable site. The pH dependent occupancy is then used to determine the microscopic pK_a values using Eq. 2.

3 Result and Discussion

In this section, we first test the convergence behavior of the hybrid MD/MCCE approach, and then apply it to study the titration behaviors of a group of alkyl amines attached to a

solvated model carbon nanoparticle; we analyze the effect of ligand density, surface curvature and ligand heterogeneity on the pK_a values of the alkyl amines.

3.1 Convergence of the hybrid MD/MCCE approach

To test the convergence of the hybrid MD/MCCE approach, we first focus on the case with a ligand density of 4.5 molecules/nm^2 (Fig. 2b), which is a moderate density of functionalization.[32] Although the simulation starts with all ($\sim$ 240) amines in the charge neutral state, we see (Fig. 3a) that the predicted fraction of charged amines at pH 9 increases to $\sim$0.2 after the first round of MCCE calculation. With a MD sampling time of 10 ns, the value continues to change significantly in the following iterations, suggesting that the snapshots collected from the MD simulations significantly impact the MCCE results. After five iterations, however, the predicted number of protonated sites has reached a plateau value of $\sim$111, which corresponds to a protonation fraction of 0.47. For other ligand densities (Fig. 2a, c), the convergence of the MD/MCCE iteration is even faster (Fig.3a); this is rather encouraging considering that the high density case involves more than 400 titratable sites.

We have also tested calculations with very short (20 ps) MD samplings for the case of low ligand density (2.3 molecules/nm^2). As shown in the **Supporting Information**, the convergence with respect to the number of iteration cycles is slower than that observed for the longer samplings, which again highlights the advantage of conducting adequate sampling to relax the ligand conformations. After 16 iterations of short sampling (i.e., cumulative sampling of merely 300 ps), the fraction of protonated sites at pH 9 approaches 0.8, which differs somewhat from the value of 0.85 obtained after 8 cycles of 10 ns MD sampling; the computed titration curves also differ somewhat for the intermediate pH values. Considering the significantly different degrees of sampling (300 ps vs. 80 ns), the observed minor differences in the computed titration properties do not indicate divergence of results. For realistic applications, we recommend long MD sampling to fully relax the ligands between iterations of MCCE calculations.

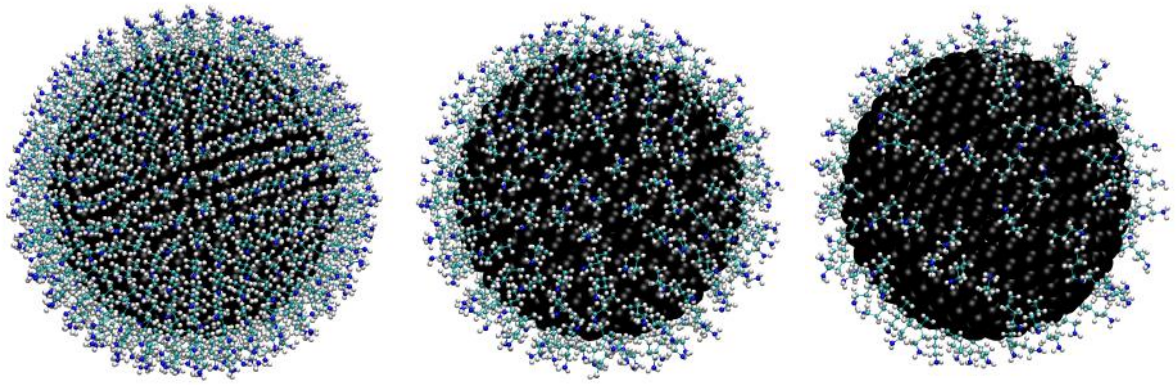

(a) (b) (c)

Figure 2: The three model carbon nanoparticles studied in this work. The nanoparticles are functionalized with n-butyl amines at a density of 9.0, 4.5 and 2.3 molecules per nm^2, respectively; these are referred to as high, moderate and low density, respectively, in the discussions.

To further evaluate the convergence behavior, we have examined how sensitive the results are to the choice of protonation pattern following MCCE pK_a calculations. Following iteration 3 of the moderate density case, we generate five configurations with different protonation patterns by randomly choosing ligands to be protonated, with the total number of protonated ligands fixed to the value predicted by the pK_a results (i.e., $\sum_i \langle P_{i,ionized} \rangle$). Starting with each configuration, the hybrid MD/MCCE calculations are carried out for another iteration, and the resulting pK_a distributions are shown in Fig. 3b. Evidently, all five configurations lead to very similar pK_a distributions with the number of protonated ligands predicted to range from 108.7 to 109.1.

3.2 Ligands on a sphere - impact of ligand density

Having understood the convergence behavior of the hybrid MD/MCCE approach, we now focus on the impact of ligand density on the computed ligand pK_a values and surface charge. The examined ligand densities are 9.0 molecules/nm^2, 4.5 molecules/nm^2 and 2.3 molecules/nm^2, which are comparable with nanoparticles synthesized in experimental studies.[32] The con-

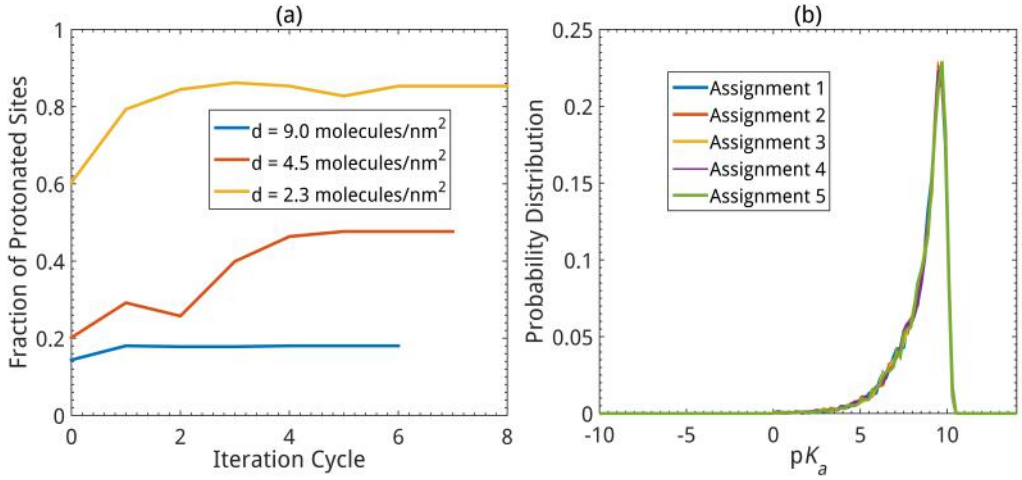

Figure 3: Convergence behaviors of the hybrid MD/MCCE protocol. (a) The fraction of predicted protonated amine sites as a function of the iteration number for different ligand densities (d). Simulations start with all amines in the deprotonated state; thus "iteration 0" is after the first cycle of MCCE calculation. (b) The distribution of computed pK_a values after one round of MD/MCCE calculation starting with five independent initial assignments of protonation pattern after iteration 3 for the moderate density case (d=4.5 molecules/nm^2).

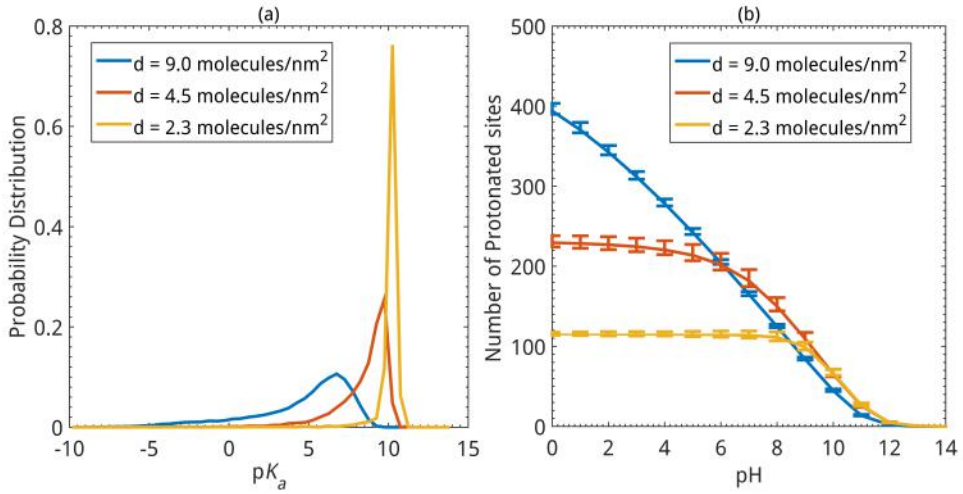

Figure 4: Dependence of computed pK_a distribution and total surface charge on the ligand density at the nanoparticle surface. (a) pK_a distributions; (b) total surface charge from the ligands as a function of pH. The error bars are estimated based on the average over 50 independent MCCE runs for snapshots taken from the last MD cycle.

verged pK_a distributions for the three cases are shown in Fig.4a, which exhibit significant differences. At low ligand density, we observe a sharp peak of distribution near the pK_a of 10, which is close to the value (10.6) for a free butylamine in aqueous solution;[80] i.e., the butylamine at the nanoparticle surface experiences little difference from solution. As the ligand density increases, the average pK_a value shifts away from the reference value, and the pK_a distribution becomes broader. In the case of the highest ligand density (9.0 molecules/nm^2), the average pK_a value shifts about 5-6 pK units from the solution reference, and the pK_a distribution reaches negative values, which indicate that some ligands remain deprotonated even at low pH. Clearly, the electrostatic interactions between neighboring ligands strongly impact the propensity of ligands to become protonated.

From the computed pK_a values, we can predict the amount of ligand charge on the nanoparticle as a function of pH. As shown in Fig. 4b, an interesting trend is that the amount of surface charge is not directly correlated with the ligand density. Under the neutral pH condition, the amount of ligand charge is in fact the highest with a moderate ligand density. At basic solution condition (pH $\sim$ 9), even the surface charge for the low-density case (2.3 molecules/nm^2) is higher than the system that has four times higher ligand density (9.0 molecules/nm^2)! Clearly, this is because high ligand density causes large pK_a shifts and therefore leads to a large number of ligands adopting the charge-neutral state. Therefore, to optimize the amount of surface charge, it is important to realize that the dependence on ligand density can be non-monotonic. Another interesting quantity in this context is the charge capacitance[81] ($\mathcal{C}$), which is defined as equilibrium charge fluctuations of a solute and is related to the derivative of the average amount of (surface) charge (Q) with respect to pH, as an example of fluctuation-dissipation relation:[82]

$$\mathcal{C} = \langle \delta^2 Q \rangle = -\frac{1}{ln10} \frac{\partial \langle Q \rangle}{\partial pH}; \tag{3}$$

note that both Q and $\mathcal{C}$ are defined here as dimensionless quantities.[81] A large charge ca-

pacitance means that the charge state of the system is sensitive to pH and external electric potentials. As seen from Fig. 4b, under the neutral pH condition, the charge capacitances of the moderate and low density systems are rather low, indicating that their surface charges remain stable with respect to perturbations in solution pH. By contrast, the high-density case has a very large charge capacitance near pH 7 ($\sim$ 17.3), suggesting that the amount of surface charge depends sensitively on pH. Depending on application, it is conceivable that either a high or a low charge capacitance is desirable and our analysis indicates that its value can be tuned by varying the ligand density. For example, correlated charge fluctuations may lead to attractive interactions between nanoparticles of similar charge, as discussed in the polyelectrolye literature;[83] whether this effect is significant for nanometer-sized particles is an interesting topic for future studies.

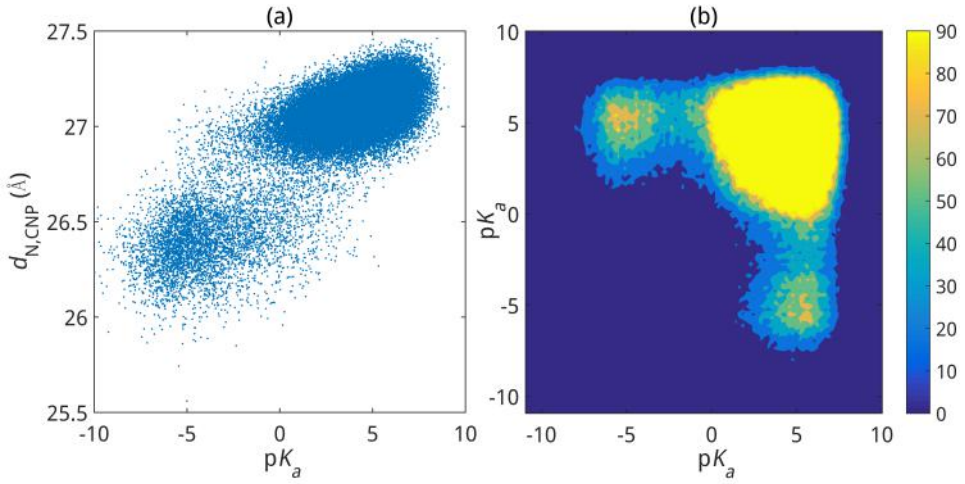

Figure 5: Factors that correlate with the computed pK_a values. (a) pK_a vs. $d_{N,CNP}$, the distance between the titratable site (amine N) and the center of the nanoparticle; (b) correlation between pK_a values of neighboring residues (the eight nearest residues measured based on the amine nitrogen atoms).

To provide further insights into factors that dictate the pK_a values, we examine the correlation between computed pK_a values with a number of variables. As shown in Fig.5a, the pK_a values are highly correlated with $d_{N,CNP}$, the distance of titratable site (amine nitrogen) to the center of the nanoparticle. Indeed, a low $d_{N,CNP}$ value indicates that the titratable site

is positioned to be spatially close to the nanoparticle surface and therefore likely surrounded by the alkyl chains of neighboring ligands rather than by solvent; desolvation leads to low pK_a values. Moreover, as shown in Fig.5b, significantly shifted pK_a values tend to be anti-correlated with the pK_a values of neighboring ligands, due largely to electrostatic coupling among neighboring sites. For a fairly broad pK_a ranges (0-8), however, there appears to be a homogeneous degree of positive correlation among neighboring pK_a values. Such broad range of correlation indicates that most titratable sites are influenced evenly by other ligands, leading to a homogeneous shift of pK_a values compared to the solution reference.

The protonated ligands are surrounded by counter ions (Cl^-), as shown by a snapshot in Fig. 6a for the example of a system of moderate ligand density (4.5 molecules/nm^2). The radial distribution function of Cl^- (Fig. 6b) can be fitted to the expected Debye-Hückel form[34] ($Ae^{-Br}/r + C$) for $r \geq 3.2$ nm, suggesting that the diffuse ion sphere starts about 1 nm away from the nanoparticle surface, as often approximated in the literature.[36,40,84] The integrated radial charges in Fig. 6c further show that the water contribution peaks around the same location, reflecting preferred orientation of water molecules due to the charged ligands. The computed radial electrostatic potential (Fig. 6d) varies rather rapidly in the region of the interface, including mild oscillations that leads to a slightly negative potential around $r \sim 2.7$ nm, reminiscent of the phenomenon of charge inversion[85] although there is only monovalent ions in the system. The negative electrostatic potential was not seen in previous simulations of a gold nanoparticle functionalized by amines,[84] likely because the previous work included only a minimal amount of Cl^- ions to neutralize the positive charge of the nanoparticle. The subtle features of the electrostatic potential makes it difficult to compare unambiguously to experimental ζ potential, which will be further investigated in future studies.

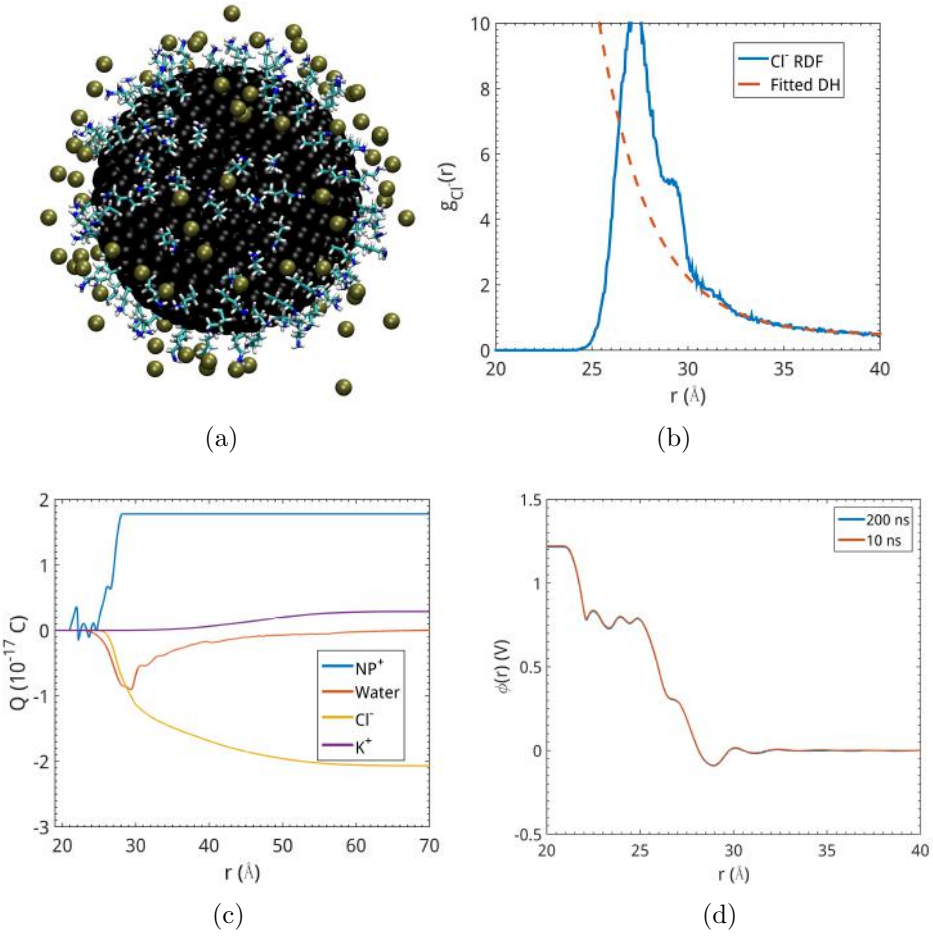

Figure 6: Distribution of charges and electrostatic potential (based on explicit solvent/ion MD simulations) around a carbon nanoparticle functionalized with n-butyl amines at a moderate surface density (4.5 molecules/nm^2). (a) A snapshot that illustrates the distribution of counter ions (Cl^-) around the positively charged nanoparticle. (b) Radial distribution of Cl^- ions around the nanoparticle; the dashed line indicates a fit to the Debye-Hückel model. (c) Integrated amount of charge for different components as a function of distance from the center of the nanoparticle. (d) Spherically averaged electrostatic potential around the nanoparticle computed by integrating over the field due to the total charges up to a given distance (Q_r): $\phi(r) = -\int_0^r E(r')dr' = -\int_0^r \frac{Q_{r'}}{4\pi\epsilon_0 r'^2}dr'$, with the potential in the bulk set to zero. The comparison of results from 10 ns and 200 ns simulations indicates that the computed electrostatic potential has properly converged.

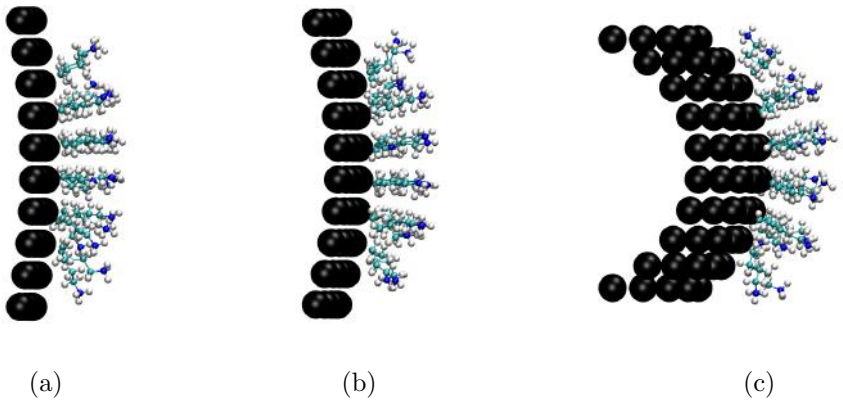

(a) (b) (c)

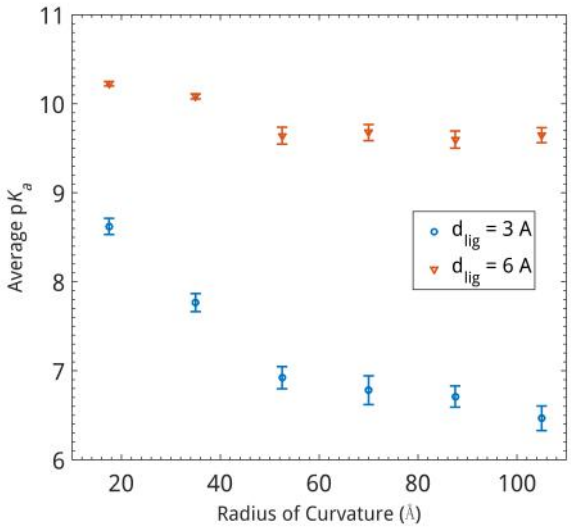

(d)

Figure 7: Dependence of pK_a on the radius of curvature of the nanosheet. (a-c) Three systems studied with radii of curvature of 87.5, 52.5 and 17.5 Å, respectively. (d) The average pK_a values for the four center ligands as functions of the radius of curvature. d_{lig} is the average distance between ligands; the value of 3 and 6 Å corresponds to the ligand density of 9.0 and 2.3 molecules per nm^2, respectively. The error bars are estimated based on the average over 50 independent MCCE runs for snapshots taken from the last MD cycle.

3.3 Ligands on a sheet - impact of surface curvature

Next, we explore how surface curvature, which is related to nanoparticle size and shape, influences the pK_a values of ligands and surface charge. To minimize computational cost, we construct a series of carbon sheets with the radius of curvature ranging from 17.5 Å to a very large value (i.e., a flat sheet); representative snapshots are shown in Fig. 7a-c. We study two ligand densities that correspond to the low and high densities studied in the last subsection; due to the finite size of the sheet, we focus on the pK_a values of the four ligands in the center.

As shown in Fig.7d, the average pK_a values depend monotonically on the radius of curvature, and the dependence is stronger at a higher ligand density; at the two limiting radii of curvature values studied here (17.5 Å and ∞), the average pK_a differ by $\sim$1 and $\sim$2 pK units at low and high ligand density, respectively. This trend is in qualitative agreement with the previous analysis of Wang et al.,[86] who observed that for a gold nanoparticle functionalized with MUA (11-mercaptoundecanoic acid) ligands, changing the nanoparticle core diameter from 7.2 nm to 4.1 nm led to a pK_a shift of $\sim$ 1 pK unit. The higher pK_a values at surfaces of higher curvature (thus a smaller radius of curvature) is due mainly to the fact that ligands avoid each other more readily at highly curved surfaces, leading to reduced electrostatic repulsion between positively charged amines.

3.4 Ligand heterogeneity

As a last example, we analyze the impact of ligand heterogeneity on their pK_a values and surface charge of the nanoparticle. For this purpose, we introduce four types of amines (with equal numbers) with different lengths of alkyl chains (butylamine, heptylamine, octylamine and decylamine); the ligands are distributed randomly on the surface of the same nanoparticle discussed above, and the amine density corresponds to the high density case studied above (see Fig. 8 for a snapshot, in which different alkyl amines are colored differently).

The computed pK_a distributions for the different types of ligands are shown in Fig. 9a;

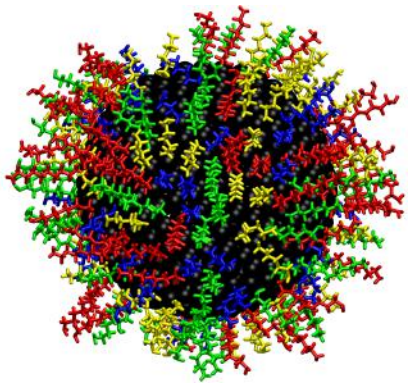

Figure 8: A snapshot of a model carbon nanoparticle functionalized with four types of alkyl amines (equal numbers of butylamine, heptylamine, octylamine and decylamine, shown in different colors); the amine density is ∼9 per nm^2, which corresponds to the high density case in Fig.2a.

compared to the homogeneous ligand case with the same ligand density (Fig. 4a), the pK_a distributions are very different and vary greatly among different amines. The decylamine ligands, which have the longest alkyl chain, have pK_a values peak at 9.5, which is a modest shift relative to the solution reference value of 10.6. On the other extreme, the shortest butylamine ligands exhibit a much broader distribution with a peak value of only ∼4, which is lower than the peak value (∼7) for the homogeneous ligand system at the same high ligand density (see Fig. 4a). The pK_a distributions for the two intermediate-length ligands are bound by those for the decylamine and butylamine ligands.

These pK_a distributions indicate that the charge state of the ligands are also affected by their chain length; longer ligands have a higher degree of conformational flexibility that allows them to avoid electrostatic repulsion from the neighboring charged groups and therefore experience lower pK_a shifts. Shorter ligands, by contrast, are more likely to be influenced by electrostatic repulsion from the nearby ligands. Moreover, titratable groups in short ligands are likely to be shielded from the solvent by nearby longer ligands, resulting in further pK_a shifts; histograms for the number of water molecules within 4 Å of the titratable site are shown for different ligands in Fig. 9b and support this hypothesis. In Fig. 9c-d, we examine the correlation between pK_a values and (i) the distance of the titratable site to the

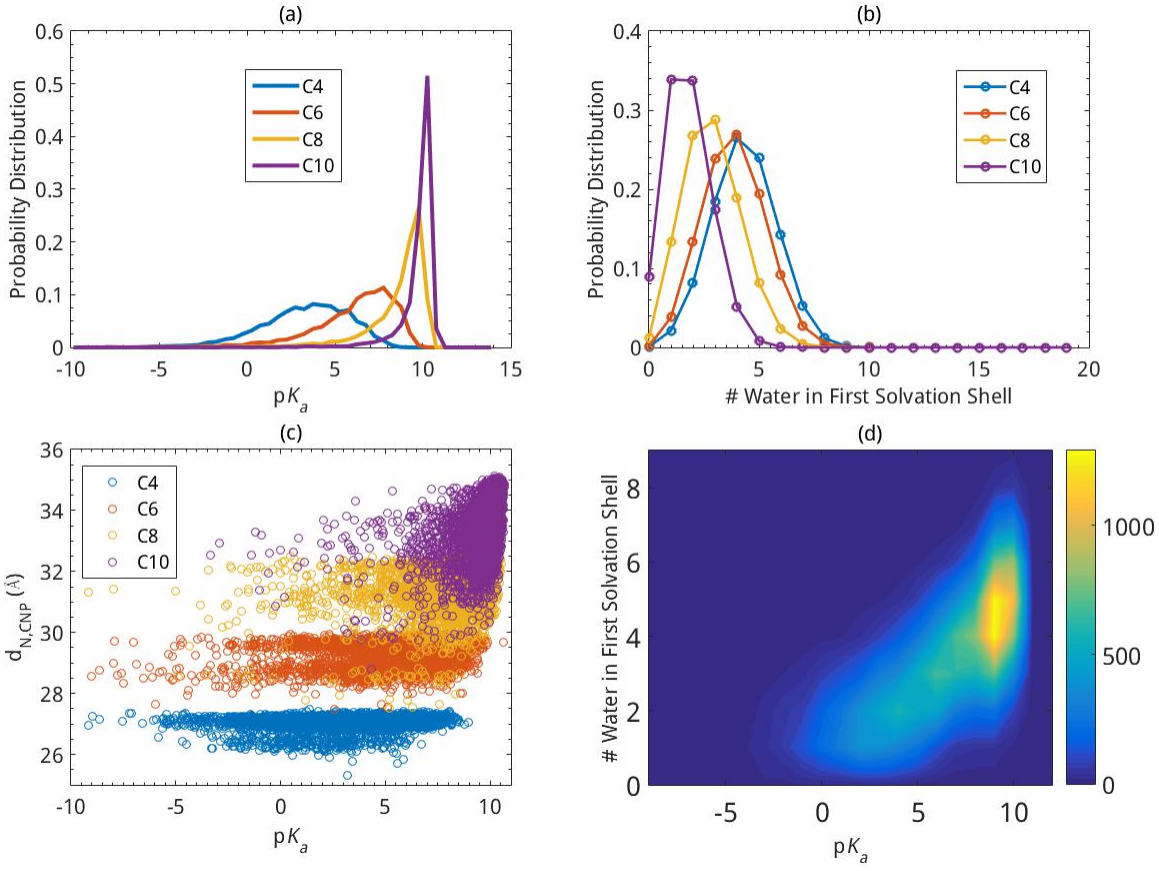

Figure 9: Properties computed for the functionalized nanoparticle shown in Fig. 8 (i.e., at a high amine density of ∼9 per nm^2). (a) pK_a distributions for the amines with different lengths of alkyl chains; (b) Distribution of the number of water molecules in the first solvation shell of the amines, computed using 50 snapshots from the last cycle of MD sampling; (c) correlation between pK_a and $d_{N,CNP}$ (compare to Fig. 5a); (d) correlation between pK_a and the number of water in the first solvation shell of the amines.

nanoparticle center $d_{N,CNP}$ and (ii) the number of water molecules in the first solvation shell of each titratable site. For decylamine, the correlation between pK_a and $d_{N,CNP}$ is fairly strong, while the correlation is much weaker (if at all) for the shorter ligands; thus unlike the case with homogeneous ligands (Fig. 5a), the location of the titratable site relative to the surface, by itself, is generally *not* a good predictor of pK_a values. The correlation between pK_a values and the local level of hydration (Fig. 9d) is stronger by comparison, highlighting the role of solvent in stabilizing the charge state of the ligand.

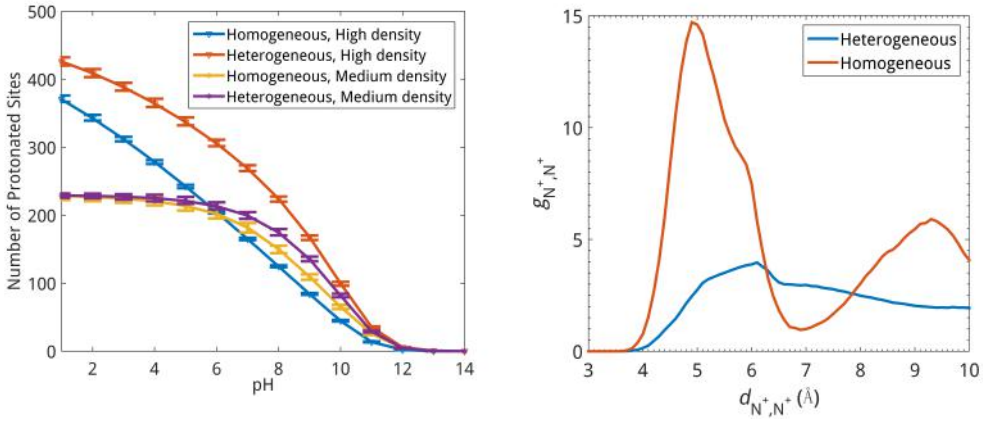

(a) (b)

Figure 10: Charge and structural properties of nanoparticles functionalized with homogeneous and heterogeneous amine ligands. (a) Comparison of the total amount of surface charge as a function of pH for the carbon nanoparticle functionalized with homogeneous and heterogeneous sets of alkyl amines at moderate (4.5 per nm^2) and high (9.0 per nm^2) amine densities. The error bars are estimated based on the average over 50 independent MCCE runs for snapshots taken from the last MD cycle. (b) Comparison of radial distribution functions for the cationic amine nitrogens (g_{N^+,N^+}) for homogeneous and heterogeneous amine cases at the high amine density.

In Fig. 10, we compare the total amount of surface charge as a function of pH for the carbon nanoparticle functionalized with homogeneous and heterogeneous sets of alkyl amines at moderate and high amine densities. At the moderate density, introducing heterogeneity into the ligands does not significantly impact the amount of surface charge at most pH values of interest. At high amine density, however, introducing heterogeneity into the chain length has a major impact on the amount of surface charge; at pH 7, for example, the

difference is almost a factor of 1.63. As discussed above, this is mostly due to the fact that the longer ligands are able to avoid the charge repulsion among neighboring residues more effectively than shorter ligands and therefore a larger number of residues are able to adopt the protonated state at neutral pH; this is confirmed by the radial distribution function for the cationic amine nitrogens, which has a substantially lower first peak at a longer distance for the case of heterogeneous ligands (Fig. 10b). Moreover, as shown in **Supporting Information**, a 1:1 butylamine and decylamine mixture at the same high amine density leads to a lower surface charge than the case shown in Fig. 10a, which includes four types of ligands with different chain lengths; therefore, introducing a high degree of chain-length heterogeneity is an effective strategy for avoiding electrostatic repulsion among neighboring charged groups.

4 Concluding Remarks

The surface charge of nanomaterials has been shown to be critical to their solution stability and interactions in the environment. To design nanomaterials that both form stable suspensions and are benign to the environment and living organisms, therefore, the ability to tune the amount of surface charge in a controlled fashion is essential. Toward this goal, understanding how the size, shape, composition of nanomaterials and their surface functionalization modulate the surface charge is important. This is not straightforward to accomplish using experiments alone due to the complexity of nanomaterials/liquid interface, especially when the interface is rough at the molecular level, which leads to uncertainties in the interpretation of experimental observables such as ζ potential and second harmonic generation intensity.

Motivated by these thoughts, we set out to explore a conceptually simple but powerful approach to computationally determine the surface charge of nanomaterials by calculating the pK_a values of titratable groups of surface ligands; the same methodology is also suited for computing reduction potentials for redox-active ligands, which may also contribute to

charge regulation. The approach integrates explicit solvent molecular dynamics simulations with a continuum electrostatic method (MCCE) to efficiently sample both configuration and chemical (protonation) spaces. The hybrid MD/MCCE protocol is complementary to constant pH MD simulations[54] for nanomaterials studies because it is able to readily handle a large number of titratable (and redox) sites, which easily reaches a value of hundreds even for moderately-sized nanomaterials. The protocol is also complementary to semi-analytical[41] and idealized model analysis[42,43] because it is, in principle, able to handle nanomaterials of arbitrary shape, composition and functionalization, provided that relevant parameters for the MD and MCCE calculations are available.

As an initial illustration, the hybrid method is applied to study the titration behavior of alkyl amines attached to a carbon-based nanoparticle; we examine the ligand pK_a value distributions as functions of ligand density, surface curvature and ligand heterogeneity, as well as the convergence behavior of the hybrid MD/MCCE simulations. The results indicate that the pK_a values converge rapidly during the iterative MD/MCCE simulations. When the ligand density on the surface is high (e.g., $\sim$9 molecules/nm^2), the pK_a values are observed to shift dramatically relative to a free amine in solution; as a result, the amount of surface charge (due to the ligands) is not a monotonic function of ligand density and actually decreases when the density is too high. Charge capacitance, which describes the stability of the surface charge, is also observed to depend on ligand density. The pK_a distribution is also modulated by the surface curvature, although the effect is relatively modest when compared to the impact of ligand density. Finally, introducing heterogeneity in ligand length is also seen to considerably alter the pK_a distribution relative to the case of homogeneous ligands at the same density.

Overall, trends in the pK_a distributions can be explained by the local level of hydration (solvent accessibility) and separation from neighboring charged groups. Although these factors are physically straightforward to understand, the findings here are significant in two ways. First, the results highlight that the charge state of surface ligands can shift signifi-

cantly relative to free ligands in solution, thus determining the proper titration state is a necessary step for any microscopic computational model that aims to probe the properties of nanomaterials and their interaction with other molecules; this is unfortunately is not routinely done in nanomaterials simulations,[84,87–89] although systematic studies along this line start to emerge.[54] Second, our analyses highlight that the charge properties of nanomaterials (e.g., ligand charge and charge capacitance) can be modulated in significant ways through several factors, such as ligand density and heterogeneity. Studies of this type can provide guidance to experimental design of nanomaterials with desired charge properties.

Finally, we acknowledge that our analysis uses a continuum electrostatic model (MCCE) that treats ions in solution in an implicit fashion (Poisson-Boltzmann); the ions are included explicitly in the explicit solvent MD simulations and therefore do contribute to modulate the configurations of the surface ligands. This is clearly an important approximation compared to explicit solvent constant pH simulations. Considering the success of the Gouy-Chapman model,[34] which is based on the same Poisson-Boltzmann framework, in interpreting surface potential of nanomaterials, our approach is likely valid at low ionic strength. On the other hand, it is possible that adsorption of ions needs to be included through, for example, a Stern model, at higher ionic strength;[34,90] the strongly adsorbed ions can also be included explicitly in the MCCE step (as was done in previous studies of Cl^- binding to proteins[91,92]), although this will considerably increase the computational cost. Another possibility is to conduct MD simulations (e.g., constant pH) with implicit solvent but explicit ions, which may also strike a balance between computational accuracy and speed; this requires, however, carefully calibrated models for the ions in the relevant implicit solvent framework. Moreover, we have used a simple carbon-based nanoparticle model in this study, which can be described as a simple low-dielectric material. For nanomaterials of complex composition, more advanced dielectric models[93] may be important to employ in the MCCE step. These technical issues need to be explored in future studies. Ultimately, it is necessary to compare computational predictions explicitly with experimental observables, such as those in electrokinetic measure-

ments. Along this line, the microscopic interpretation of ζ potential is not straightforward for nanomaterials of complex shape and surface roughness, thus it might be preferable to compute mobility from simulations and compare to experimental measurement.[94]

Acknowledgement

The work has been supported by the grant from the National Science Foundation CHE-1503408. Computational resources from the Extreme Science and Engineering Discovery Environment (XSEDE), which is supported by NSF grant number OCI-1053575, are greatly appreciated; computations are also supported in part by NSF through a major instrumentation grant (CHE-0840494) to the Chemistry department.

Supporting Information Available

Convergence of structural properties and pK_a during the MD simulations, and additional control simulations for a nanoparticle functionalized with different sets of homogeneous and heterogeneous alkyl amines. This material is available free of charge via the Internet at `http://pubs.acs.org/`.

References

(1) Arico, A. S.; Bruce, P.; Scrosati, B.; Tarascon, J. M.; Van Schalkwijk, W. Nanostructured Materials for Advanced Energy Conversion and Storage Devices. *Nat. Mater.* **2005**, *4*, 366–377.

(2) Khin, M. M.; Nair, S. A.; Babu, V. J.; Murugan, R.; Ramakrishna, S. A Review on Nanomaterials for Environmental Remediation. *Energy Environ. Sci.* **2012**, *5*, 8075.

(3) Shannon, M. A.; Bohn, P. W.; M, M. E.; Georgiadis, J. G.; Marinas, B. J.; Mayes, A. M.

Science and Technology for Water Purification in the Coming Decades. *Nature* **2008**, *452*, 301.

(4) Lee, K. P.; Arnot, T. C.; Mattia, D. A Review of Reverse Osmosis Membrane Materials for Desalination-Development to Date and Future Potential. *J. Memb. Sci.* **2011**, *370*, 1–22.

(5) Huang, X.; El-Sayed, E. H.; Qian, W.; El-Sayed, M. A. Cancer Cell Imaging and Photothermal Therapy in the Near-infrared Region by Using Gold Nanorods. *J. Am. Chem. Soc.* **2006**, *128*, 2115.

(6) Gao, X. H.; Cui, Y. Y.; Leveson, R. M.; Chung, L. W. K.; Nie, S. In vivo Cancer Targeting and Imaging with Semiconductor Quantum Dots. *Nat. Biotechnol.* **2004**, *22*, 969.

(7) Michalet, X.; Pinaud, F. F.; Bentolila, L. A.; Tsay, J. M.; Doose, S.; Li, J. J.; Sundaresan, G.; Wu, A. M.; Gambhir, S. S.; Weiss, S. Quantum Dots for Live Cells, in vivo Imaging, and Diagnostics. *Science* **2005**, *307*, 538–544.

(8) Ferrari, M. Cancer Nanotechnology: Opportunities and Challenges. *Nat. Rev. Cancer* **2005**, *5*, 161–171.

(9) Langer, R.; Tirrell, D. A. Designing Materials for Biology and Medicine. *Nature* **2004**, *428*, 487–492.

(10) Giljohann, D. A.; Seferos, D. S.; Daniel, W. L.; Massich, M. D.; Patel, P. C.; Mirkin, C. A. Gold Nanoparticles for Biology and Medicine. *Angew. Chem. Int. Ed.* **2010**, *49*, 3280–3294.

(11) Jain, S.; Hirst, D. G.; O'Sullivan, J. M. Gold Nanoparticles as Novel Agents for Cancer Therapy. *Br. J. Radiol.* **2012**, *85*, 101.

(12) Shipway, A. N.; Karz, E.; Willner, I. Nanoparticle Arrays on Surfaces for Electronic, Optical, and Sensor Applications. *ChemPhysChem* **2000**, *1*, 18–52.

(13) Talapin, D. V.; Steckel, J. Quantum-dot Light-emitting Devices. *MRS Bull.* **2013**, *38*, 685.

(14) Yildirimer, L.; Thanh, N. T. K.; Loizidou, M.; Seifalian, A. M. Toxicological Considerations of Clinically Applicable Nanoparticles. *Nano Today* **2011**, *6*, 586.

(15) Roco, M., Bainbridge, W. S., Eds. *Nanotechnoloy: Societal Implications I; Maximizing Benefits for Humanity*; Springer: Dordrecht, The Netherlands, 2007.

(16) Sayes, C. M.; Gobin, A. M.; Ausman, K. D.; Mendez, J.; West, J. L.; Colvin, V. L. Nano-C-60 Cytotoxicity is due to Lipid Peroxidation. *Biomaterials* **2005**, *26*, 7687–7595.

(17) Ge, C. C.; Du, J. F.; Zhao, L. N.; Wang, L. M.; Liu, Y.; Li, D. H.; Yang, Y. L.; Zhou, R. H.; Zhao, Y. L.; Z. F. Chai et al., Binding of Blood Proteins to Carbon Nanotubes Reduces Cytotoxicity. *Proc. Natl. Acad. Sci. USA* **2011**, *108*, 16968–16973.

(18) Maurer-Jones, M. A.; Gunsolus, I. L.; Murphy, C. J.; Haynes, C. L. Toxicity of Engineered Nanoparticles in the Environment. *Anal. Chem.* **2013**, *85*, 3036–3049.

(19) Nel, A. E.; Madler, L.; Velegol, D.; Xia, T.; Hoek, E. M. V.; Somasundaran, P.; Klaessig, F.; Castranova, V.; Thompson, M. Understanding Biophysicochemical Interactions at the Nano-bio Interface. *Nat. Mater.* **2009**, *8*, 543–557.

(20) Kim, S. T.; Saha, K.; Kim, C.; Rotello, V. M. The Role of Surface Functionality in Determining Nanoparticle Cytotoxicity. *Acc. Chem. Res.* **2012**, *46*, 681–691.

(21) Kuech, T. R.; Hamers, R. J.; Pedersen, J. A. In *Engineered Nanoparticles and the Environment: Biophysicochemical Processes and Biotoxicity*; Xing, B., Vectis, C. D., Senesi, N., Eds.; Biophysico-chemical Processes in Environmental Systems; Willey, 2016;

Vol. 4; Chapter Chemical Transformations of Metal, Metal Oxide, and Metal Chalcogenide Nanomaterials in the Environment.

(22) Murphy, C. J.; Vartanian, A. M.; Geiger, F. M.; Hamers, R. J.; Pedersen, J.; Cui, Q.; Haynes, C. L.; Carlson, E. E.; Hernandez, R.; R. D. Klaper et al., Biological Responses to Engineered Nanomaterials: Needs for the Next Decade. *ACS Central Sci.* **2015**, *1*, 117–123.

(23) Cui, Q.; Hernandez, R.; Mason, S.; T. Frauenheim,; Pedersen, J.; Geiger, F. M. Sustainable Nanotechnology: Opportunities and Challenges for Theoretical/Computational Studies. *J. Phys. Chem. B* **2016**, *120*, 7297–7306.

(24) Monopoli, M. P.; Aberg, C.; Salvati, A.; Dawson, K. A. Biomolecular Coronas Provide the Biological Identity of Nanosized Materials. *Nat. Nanotech.* **2012**, *7*, 779–786.

(25) B, B. W.; Zhang, L.; Bae, S. C.; Granick, S. Nanoparticle-induced Surface Reconstruction of Phospholipid Membranes. *Proc. Natl. Acad. Sci. USA* **2008**, *105*, 18171.

(26) Moghadam, B. Y.; Hou, W. C.; Corredor, C.; Westerhoff, P.; Posner, J. D. Role of Nanoparticle Surface Functionality in the Disruption of Model Cell Membranes. *Langmuir* **2012**, *28*, 16319.

(27) Carney, R. P.; Astier, Y.; Carney, T. M.; Voitchovsky, K.; Silva, P. H. J.; Stellacci, F. Electrical Method to Quantify Nanoparticle Interaction with Lipid Bilayers. *ACS Nano* **2013**, *7*, 932.

(28) Van Lehn, R. C.; Alexander-Katz, A. Free Energy Change for Insertion of Charged, Monolayer-protected Nanoparticles into Lipid Bilayers. *Soft Matter* **2014**, *10*, 648.

(29) Feng, Z. V.; Gunsolus, I. L.; Qiu, T. A.; Hurley, K. R.; Nyberg, L. H.; Frew, H.; Johnson, K. P.; Vartanian, A. M.; Jacob, L. M.; S. E. Lohse et al., Impacts of Gold Nanopar-

ticle Charge and Ligand Type on Surface Binding and Toxicity to Gram-Negative and Gram-Positive Bacteria. *Chem. Sci.* **2015**, *6*, 5186–5196.

(30) Dominguez, G. A.; Lohse, S. E.; Torelli, M. D.; Murphy, C. J.; Hamers, R. J.; Orr, G.; Klaper, R. D. Effects of Charge and Surface Ligand Properties of Nanoparticles on Oxidative Stress and Gene Expression within the Gut of *Daphnia magna*. *Aquatic Toxicology* **2015**, *162*, 1 – 9.

(31) Ullmann, G. M. Relations between Protonation Constants and Titration Curves in Polyprotic Acids: A Critical View. *J. Phys. Chem. B* **2003**, *107*, 1263–1271.

(32) Torelli, M. D.; Putans, R. A.; Tan, Y. Z.; Lohse, S. E.; Murphy, C. J.; Hamers, R. J. Quantitative Determination of Ligand Densities on Nanomaterials by X-ray Photoelectron Spectroscopy. *ACS Appl. Mater. & Inter.* **2015**, *7*, 1720–1725.

(33) Gmür, T. A.; Goel, A.; Brown, M. A. Quantifying Specific Ion Effects on the Surface Potential and Charge Density at Silica NanoparticleAqueous Electrolyte Interfaces. *J. Phys. Chem. C* **2016**, *120*, 16617–16625.

(34) Barrat, J.-L.; Hansen, J.-P. *Basic Concepts for Simple and Complex Liquids*; Cambridge University Press: Cambridge, UK, 2003.

(35) Brown, M. A.; Abbas, Z.; Kleibert, A.; Green, R. G.; Goel, A.; May, S.; Squires, T. M. Determination of Surface Potential and Electrical Double-Layer Structure at the Aqueous Electrolyte-Nanoparticle Interface. *Phys. Rev. X* **2016**, *6*, 011007.

(36) Kimura, K.; Takashima, S.; Ohshima, H. Molecular Approach to the Surface Potential Estimate of Thiolate-Modified Gold. *J. Phys. Chem. B* **2002**, *106*, 7260–7266.

(37) Makino, K.; Ohshima, H. Electrophoretic Mobility of a Colloidal Particle with Constant Surface Charge Density. *Langmuir* **2010**, *26*, 18016–18019.

(38) Troiano, J. M.; Olenick, L. L.; Kuech, T. R.; Melby, E. S.; Hu, D.; Lohse, S. E.; Mensch, A. C.; Dogangun, M.; Vartanian, A. M.; M. D. Torelli et al., Direct Probes of 4-nm Diameter Gold Nanoparticles Interacting with Supported Lipid Bilayers. *J. Phys. Chem. C* **2015**, *119*, 534.

(39) Troiano, J. M.; Kuech, T. R.; Vartanian, A. M.; Torelli, M. D.; Sen, A.; Jacob, L. M.; Hamers, R. J.; Murphy, C. J.; Pedersen, J. A.; Geiger, F. M. On Electronic and Charge Interference in Second Harmonic Generation Responses from Gold Metal Nanoparticles at Supported Lipid Bilayers. *J. Phys. Chem. C* **2016**, *120*, 20659–20667.

(40) Kumal, R. R.; Karam, T. E.; Haber, L. H. Determination of the Surface Charge Density of Colloidal Gold Nanoparticles Using Second Harmonic Generation. *J. Phys. Chem. C* **2015**, *119*, 16200–16207.

(41) Wang, D.; Nap, R. J.; Lagzi, I.; Kowalczyk, B.; Han, S.; Grzybowski, B. A.; Szleifer, I. How and Why Nanoparticle's Curvature Regulates the Apparent pKa of the Coating Ligands. *J. Am. Chem. Soc.* **2011**, *133*, 2192–2197, PMID: 21280574.

(42) Arnaud, C.; Marianne, S.; Fabrice, C.; Serge, S. Surface Charging Behavior of Nanoparticles by Considering Site Distribution and Density, Dielectric constant and pH Changes - a Monte Carlo Approach. *Phys. Chem. Chem. Phys.* **2015**, *17*, 4346–4353.

(43) Clavier, A.; Carnal, F.; Stoll, S. Effect of Surface and Salt Properties on the Ion Distribution around Spherical Nanoparticles: Monte Carlo Simulations. *J. Phys. Chem. B* **2016**, *120*, 7988–7997, PMID: 27459187.

(44) Alexov, E.; Mehler, E. L.; Baker, N.; Baptista, A. M.; Huang, Y.; Milletti, F.; Nielsen, J. E.; Farrell, D.; Carstensen, T.; M. H. M. Olsson et al., Progress in the Prediction of pK(a) Values in Proteins. *Proteins: Struct. Funct. & Bioinf.* **2011**, *79*, 3260–3275.

(45) Antosiewicz, J.; J. A. McCammon,; Gilson, M. K. Prediction of pH-dependent Properties of Proteins. *J. Mol. Biol.* **1994**, *238*, 415–436.

(46) Warshel, A.; Sharma, P. K.; Kato, M.; Parson, W. W. Modeling Electrostatic Effects in Proteins. *Biochim. Biophys. Acta* **2006**, *1764*, 1647–1676.

(47) Bashford, D.; Karplus, M. pK_a's of Ionizable Groups in Proteins: Atomic Detail from a Continuum Electrostatic Model. *Biochem.* **1990**, *29*, 10219–10225.

(48) Georgescu, R. E.; Alexov, E. G.; Gunner, M. R. Combining Conformational Flexibility and Continuum Electrostatics for Calculating pKas in Proteins. *Biophys. J.* **2002**, *83*, 1731 – 1748.

(49) Donnini, S.; Tegeler, F.; Groenhof, G.; Grubmuller, H. Constant pH Molecular Dynamics in Explicit Solvent with λ-Dynamics. *J. Chem. Theory Comput.* **2011**, *7*, 1962–1978.

(50) Itoh, S. G.; Damjanović, A.; Brooks, B. R. pH Replica-exchange Method Based on Discrete Protonation States. *Proteins* **2011**, *79*, 3420–3436.

(51) Goh, G. B.; Knight, J. L.; C. L. Brooks III, Constant pH Molecular Dynamics Simulations of Nucleic Acids in Explicit Solvent. *J. Chem. Theory Comput.* **2012**, *8*, 36–46.

(52) Wallace, J. A.; Shen, J. K. Continuous Constant pH Molecular Dynamics in Explicit Solvent with pH-Based Replica Exchange. *J. Chem. Theory Comput.* **2011**, *7*, 2617–2629.

(53) Chen, Y. J.; Roux, B. Constant-pH Hybrid Nonequilibrium Molecular Dynamics Monte Carlo Simulation Method. *J. Chem. Theory Comput.* **2015**, *11*, 3919–3931.

(54) Koivisto, J.; Chen, X.; Donnini, S.; Lahtinen, T.; Häkkinen, H.; Groenhof, G.; Pettersson, M. AcidBase Properties and Surface Charge Distribution of the Water- Soluble $Au_{102}(pMBA)_{44}$ Nanocluster. *J. Phys. Chem. C* **2016**, *120*, 10041–10050.

(55) Simonson, T.; Roux, B. Concepts and Protocols for Electrostatic Free Energies. *Mol. Simul.* **2016**, *42*, 1090–1101.

(56) Donnini, S.; Ullmann, R. T.; Groenhof, G.; Grubmuller, H. Charge-neutral Constant pH Molecular Dynamics Simulations Using a Parsimonious Proton Buffer. *J. Chem. Theory Comput.* **2016**, *12*, 1040–1051.

(57) Chen, W.; Shen, J. K. Effects of System Net Charge and Electrostatic Truncation on All-Atom Constant pH Molecular Dynamics. *J. Comput. Chem.* **2014**, *35*, 1986–1996.

(58) Burgi, R.; Kollman, P. A.; W. F. van Gunsteren, Simulating Proteins at Constant pH: An Approach Combining Molecular Dynamics and Monte Carlo Simulation. *Proteins: Struct. Funct. & Bioinf.* **2002**, *47*, 469–480.

(59) Baptista, A. M.; Teixeira, V. H.; Soares, C. M. Constant-pH Molecular Dynamics Using Stochastic Titration. *J. Chem. Phys.* **2002**, *117*, 4184–4200.

(60) Ziebarth, J. D.; Wang, Y. M. Understanding the Protonation Behavior of Linear Polyethylenimine in Solutions through Monte Carlo Simulations. *Biomacro.* **2010**, *11*, 29–38.

(61) Teixeira, V. H.; Vila-Vicosa, D.; Reis, P. B. P. S.; Machuqueiro, M. pKa Values of Titrable Amino Acids at the Water/Membrane Interface. *J. Chem. Theory Comput.* **2016**, *12*, 930–934.

(62) Santos, H. A. F.; Vila-Vicosa, D.; Teixeira, V. H.; Baptista, A. M.; Machuqueiro, M. Constant-pH MD Simulations of DMPA/DMPC Lipid Bilayers. *J. Chem. Theory Comput.* **2015**, *11*, 5973–5979.

(63) Song, Y.; Mao, J.; Gunner, M. R. MCCE2: Improving Protein pKa Calculations with Extensive Side Chain Rotamer Sampling. *J. Comput. Chem.* **2009**, *30*, 2231–2247.

(64) Landau, D. P.; Binder, K. *A Guide to Monte Carlo Simulations in Statistical Physics*; Cambridge University Press: Cambridge, UK, 2000.

(65) Baker, N. A.; Sept, D.; Joseph, S.; Holst, M. J.; McCammon, J. A. Electrostatics of Nanosystems: Application to Microtubules and the Ribosome. *Proc. Natl. Acad. Sci. USA* **2001**, *98*, 10037–10041.

(66) Schutz, C. N.; Warshel, A. What are the Dielectric "Constants" of Proteins and How to Validate Electrostatic Models? *Proteins: Struct. Funct. & Gene.* **2001**, *44*, 400–417.

(67) Archontis, G.; Simonson, T. Dielectric Relaxation in an Enzyme Active Site: Molecular Dynamics Simulations Interpreted with a Macroscopic Continuum Model. *J. Am. Chem. Soc.* **2001**, *123*, 11047–11056.

(68) Archontis, G.; Simonson, T. Proton Binding to Proteins: A Free-energy Component Analysis using a Dielectric Continuum Model. *Biophys. J.* **2005**, *88*, 3888–3904.

(69) Vanommeslaeghe, K.; Hatcher, E.; Acharya, C.; Kundu, S.; Zhong, S.; Shim, J.; Darian, E.; Guvench, O.; Lopes, P.; I. Vorobyov et al., CHARMM General Force Field: A Force Field for Drug-Like Molecules Compatible with the CHARMM All-Atom Additive Biological Force Fields. *J. Comput. Chem.* **2010**, *31*, 671–690.

(70) Huang, J.; A. D. MacKerell Jr., CHARMM36 All-atom Additive Protein Force Field: Validation Based on Comparison to NMR Data. *J. Comput. Chem.* **2013**, *34*, 2135–2145.

(71) Jorgensen, W. L.; Chandrasekhar, J.; Madura, J. D.; Impey, R. W.; Klein, M. L. Comparison of Simple Potential Functions for Simulating Liquid Water. *J. Chem. Phys.* **1983**, *79*, 926–935.

(72) MacKerell, A. D.; Bashford, D.; Bellott, M.; Dunbrack, R. L.; Evanseck, J. D.; Field, M. J.; Fischer, S.; Gao, J.; Guo, H.; S. Ha et al., All-Atom Empirical Potential

for Molecular Modeling and Dynamics Studies of Proteins. *J. Phys. Chem. B* **1998**, *102*, 3586–3616.

(73) Nosé, S. A Unified Formulation of the Constant Temperature Molecular Dynamics Methods. *J. Chem. Phys.* **1984**, *81*, 511–519.

(74) Hoover, W. G. Canonical Dynamics: Equilibrium Phase-space Distributions. *Phys. Rev. A* **1985**, *31*, 1695–1697.

(75) Darden, T.; York, D.; Pedersen, L. Particle Mesh Ewald: An N log (N) Method for Ewald Sums in Large Systems. *J. Chem. Phys.* **1993**, *98*, 10089–10092.

(76) Ryckaert, J.-P.; Ciccotti, G.; Berendsen, H. J. C. Numerical Integration of the Cartesian Equations of Motion of a System with Constraints: Molecular Dynamics of n-alkanes. *J. Comput. Phys.* **1977**, *23*, 327–341.

(77) Goh, G. B.; Laricheva, E.; C. L. Brooks III, Uncovering pH-Dependent Transient States of Proteins with Buried Ionizable Residues. *J. Am. Chem. Soc.* **2014**, *136*, 8496–8499.

(78) Brooks, B. R.; C. L. Brooks III,; Mackerell, A. D.; Nilsson, L.; Petrella, R. J.; Roux, B.; Won, Y.; Archontis, G.; Bartels, C.; S. Boresch et al., CHARMM: The Biomolecular Simulation Program. *J. Comput. Chem.* **2009**, *30*, 1545–1614.

(79) Phillips, J. C.; Braun, R.; Wang, W.; Gumbart, J.; Tajkhorshid, E.; Villa, E.; Chipot, C.; Skeel, R. D.; Kale, L.; Schulten, K. Scalable Molecular Dynamics with NAMD. *J. Comput. Chem.* **2005**, *26*, 1781–1802.

(80) Lide, D. R., Ed. *CRC Handbook Chemistry and Physics*, 85th ed.; CRC Press, 2005.

(81) Lund, M.; Jönsson, B. Charge Regulation in Biomolecular Solution. *Q. Rev. Biophys.* **2013**, *46*, 265–281.

(82) Kubo, R.; Toda, M.; Hashitsume, N. *Statistical Physics II: Nonequilibrium Statistical Mechanics*; Springer, 2003.

(83) Barrat, J. L.; Joanny, J. F. Theory of Polyelectrolyte Solutions. *Adv. Chem. Phys.* **1996**, *94*, 1–66.

(84) Heikkilä, E.; Gurtovenko, A. A.; Martinez-Seara, H.; Häkkinen, H.; Vattulainen, I.; Akola, J. Atomistic Simulations of Functional $Au_{144}(SR)_{60}$ Gold Nanoparticles in Aqueous Environment. *J. Phys. Chem. C* **2012**, *116*, 9805–9815.

(85) Grosberg, A. Y.; Nguyen, T. T.; Shklovskii, B. I. *Colloquium*: The Physics of Charge Inversion in Chemical and Biological Systems. *Rev. Mod. Phys.* **2002**, *74*, 329–345.

(86) Wang, D. W.; Nap, R. J.; Lagzi, I.; Kowalczyk, B.; Han, S. B.; Grzybowski, B. A.; Szleifer, I. How and Why Nanoparticle's Curvature Regulates the Apparent pK(a) of the Coating Ligands. *J. Am. Chem. Soc.* **2011**, *133*, 2192–2197.

(87) Bolintineanu, D. S.; Lane, J. M. D.; Grest, G. S. Effects of Functional Groups and Ionization on the Structure of Alkanethiol-Coated Gold Nanoparticles. *Langmuir* **2014**, *30*, 11075–11085.

(88) Martinez-Seara, E. H. H.; Gurtovenko, A. A.; Javanainen, M.; Häkkinen, H.; Vattulainen, I.; Akola, J. Cationic Au Nanoparticle Binding with Plasma Membrane-like Lipid Bilayers: Potential Mechanism for Spontaneous Permeation to Cells Revealed by Atomistic Simulations. *J. Phys. Chem. C* **2014**, *118*, 11131–11141.

(89) Batista, C. A. S.; Larson, R. G.; Kotov, N. A. Nonadditivity of Nanoparticle Interactions. *Science* **2015**, *350*, 176.

(90) Zhang, L.; Yethiraj, A.; Cui, Q. Free Energy Calculations for the Peripheral Binding of Proteins/Peptides to an Anionic Membrane. I. Implicit Membrane Models. *J. Chem. Theory Comput.* **2014**, *10*, 2845–2859.

(91) Song, Y. F.; Gunner, M. R. Using Multiconformation Continuum Electrostatics to Com-

pare Chloride Binding Motifs in alpha-Amylase, Human Serum Albumin, and Omp32. *J. Mol. Biol.* **2009**, *387*, 840–856.

(92) Song, Y. F.; Gunner, M. R. Halorhodopsin Pumps Cl- and Bacteriorhodopsin Pumps Protons by a Common Mechanism that Uses Conserved Electrostatic Interactions. *Proc. Natl. Acad. Sci. USA* **2014**, *111*, 16377–16382.

(93) Bonthuis, D. J.; Gekle, S.; Netz, R. R. Profile of the Static Permittivity Tensor of Water at Interfaces: Consequences for Capacitance, Hydration Interaction and Ion Adsorption. *Langmuir* **2012**, *28*, 7679–7694.

(94) Ge, Z. P.; Wang, Y. Estimation of Nanodiamond Surface Charge Density from Zeta Potential and Molecular Dynamics Simulations. *J. Phys. Chem. B* **2016**, *ASAP*.

TOC Graphics